Responses to the comments from the reviewer 2

Paper no.: amtd-8-10097-2015

We would like to express our sincere thanks to the reviewers for the invaluable comments which help improve our manuscript. Our responses are as follows:
(Changes in the revised manuscript are highlighted in blue)

1. The paper presents a statistical study of calibration parameters for frequency domain range interferometry using the Chung-Li VHF radar. The method is similar to astronomical radio imaging using spaced receivers to obtain high resolution images. However, instead of angular resolution, the method goes after range resolution with spaced frequencies. As with radio astronomical imaging, some assumptions of sparseness of the image is required to obtain super-resolution of the target. In this case, the assumption is that the target can consist of narrow layers smaller than occupied bandwidth would otherwise allow nDelta R = $c/(2(f_max-f_min)$.

   Super-resolution is an important topic of research for radar engineering. However, the topic is not easy. As stated in the paper, good calibration of the system is important. Another important topic is regularization of the imaging, and the effects that it can have on the data products.

Response: Multifrequency RIM is indeed similar to astronomical radio imaging using spacing receivers, except that RIM uses spaced frequencies. In fact, spacing-receiver technique has also been applied to observation of the atmosphere using the VHF-MST radar, termed spatial domain interferometry or coherent radar imaging (CRI) in later time.

Indeed, calibration of the system and regularization of the imaging are important to produce high-quality and reliable outcomes. In this study, we employed the calibration approach developed in our previous work to obtain the optimal calibration parameters to improve the imaging, thereby verifying the general usability of RIM for the upgraded Chung-Li radar.

2. The paper presents a large statistical study of the calibration parameters and provides several examples of range imaging data products. The paper also attempts to explain the features in the histograms for these parameters, but fails to provide a conclusive explanation to the features in the data.

Response: We give some explanations of the calibration results, although some still confuse us. For example, the difference in σ_z value between the first four cases can be attributed to the uses of different pulse shapes and filter bandwidths; the increase of time delay/range delay with time could be associated with the aging of cable lines or some components in the radar system. With the calibrated σ_z value and range delay, we can recover the range power of the atmospheric structure in more detail, no matter what causes of the biased σ_z value or range delay are. Two puzzles are: (1) the different in range/time delay (transform by phase bias) between the uses of 1-us and 2-us pulse lengths, and (2) the difference of range/time delay between precipitation and atmospheric echoes. We give a conjecture of the second puzzle in the last paragraph of Sect. 4.1.

We did not provide explanations for all the calibration results. It may not be easy to clarify all problems in this paper with the present data; some open questions need further examinations with other methods or auxiliary instruments. We contribute the calibration approach to a practical use of RIM for atmospheric studies, in spite of diversified changes

of radar characteristics and atmospheric conditions.

3. The paper would greatly benefit from more information on the imaging method. In current form, the imaging algorithm is not very well described. The authors state that they utilize the Capon method. At the same time, there is also a cost function, which resembles Tikhonov regularization using first order differences (equation 1) of neighbouring image pixels in range. How are these two methods combined? It is also not clear if the range weighting function parametrized using $nsigma_z$ is part of the radar target model or if it is used to model the range ambiguity due to transmit pusle shape and receiver filters, or perhaps both.

Response:

- *… the imaging algorithm is not very well described…*

The Capon method was first applied to the VHF-MST radar in 1998 (Palmer et al.) and also addressed well in many papers (see the introduction and reference list). To save the space, we intend not to repeat it again. We focus on the function of our calibration approach and validate the RIM technique for the Chung-Li radar system.

- *…at the same time, there is also a cost function,…*

We are sorry that we did not think of the method of Tikhonov regularization when used Eq. (1) as an estimator in the calibration process. Eq. (1) is simply a mean-square error estimator, which is for finding the minimum difference between two data sets, as described in the last paragraph of Sect. 2. In our calibration process, by changing iteratively the two variables - range delay and standard deviation of range-weighting function, we can find a minimum difference between the two data sets, which is the condition we seek. Eq. (1) does not go into the processing of Tikhonov regularization.

- *…It is also not clear if the range weighting function…*

The range weighting function is defined by the convolution of transmitted pulse shape and receiver filter impulse response, giving the weighted contribution of individual scatterers in the range direction of the radar volume. A standard Gaussian function is commonly used to approach the shape of the range-weighting function, and the standard deviation σ_r is $0.35c\tau/2$, where c the speed of the light, τ is the pulse width. Our definition of Gaussian function (sect. 3.1, the first paragraph) is slightly different from the standard Gaussian function, our σ_z equals to $\sqrt{2}\sigma_r$.

According to the definition, σ_z or σ_r is not for the radar target model. We do not need to know the shape or distribution of radar target before range imaging. Without noise in the data, the theoretical value of σ_z or σ_r is able to mitigate the range-weighting effect. In fact, we have addressed this issue in our previous study (Chen et al, 2014b in the reference list). In that study we used a rectangular 2-us pulse length and its matched filter, and the calibrated σ_z at high SNR was about 150 m, which was very close to the theoretical value ($\sqrt{2}\sigma_r = \sqrt{2}\ 0.35c\tau/2 \cong 148$ m).

It is expected that the calibrated σ_z also varies with the imaging method, especially at low SNR if the method is sensitive to noise, like the Capon method. Namely, the SNR-dependent σ_z may vary with the imaging method. We have given more information of range-weighting function in the last paragraph, Sect. 3.1.

4. Line 19 (on P10102) states a threshold of -9 dB for power. What is this relative to? It should be stated. The negative value implies that this coherent integration and pulse compression is used, but what is the signal procesing gain?

Response: It is the signal-to-noise ratio (SNR), not power. The noise power was estimated for each calculation, and deducted from the power of the received echoes to obtain the signal power. SNR is estimated as $10\times\log_{10}$(signal power/noise power), giving the unit of dB. The negative value of SNR in dB means that the signal power is smaller than the noise power. The absolute amplitude of radar echoes was not calibrated in the experiment; however, the unit of noise and echo power is not important in the estimate of SNR.

5. The paper states that $nsigma_z$ is dependent on SNR and approaches 100 m with high SNR. The paper does not explain why this is. Perhaps the explanation is the following: The utilized experiments in most cases span 1.5 MHz of bandwidth. Due to the used pulse lengths and frequency spacings, this bandwidth is actually fully populated. One can therefore obtain a non-imaging resolution simply by using $c/(2B)$, where $c=3e8$ and $B=1.5e6$, which happens to be 100 m. The Tikhonov first order differences cost function encourages smoothness of the image. In low SNR cases, there is nothing to image and therefore the solutions tend towards smooth solutions with large $nsigma_z$, and in high SNR cases $nsigma_z$ approaches the intrinsic range resolution of 1.5 MHz.

Response: We have added more information of range-weighting function in the last paragraph of Sect. 3.1 to explain the value of σ_z at high SNR. An explanation of the SNR-dependent σ_z is also given, partly referring to the comment from the reviewer. As the noise increases, the imaging results retrieved by the Capon method deteriorate because the performance of Capon method is subject to signal-to-noise ratio (SNR). In the lower SNR cases, as the reviewer reminds, there is nothing to image. The range-weighting effect become less and less important as the SNR decreases, therefore a larger value of σ_z is obtained from the calibration process.

As mentioned in the point 2, the range weighting function is defined by the convolution of transmitted pulse shape and receiver filter impulse response. The σ_z value at very high SNR or approximately at the peak of the σ_z histogram can model the range-weighting function well. In Fig. 1b, the σ_z value approaches 100 m at high SNR, which is due to the Gaussian pulse shape used in the experiment. If a rectangular pulse shape was employed, the σ_z value should approach ~74 m, the theoretical value. Table 1 lists the peak locations of σ_z histograms for various radar parameters. Fig. 1 presents only a special case.

We would like to mention again: to find the dependent relationship between σ_z and SNR for a better illustration of imaging is the function of the calibration approach. Such a relationship varies with the radar parameters used; it is also expected to vary with the retrieval method (the so-called range imaging model?), although we haven't examined this issue yet.

6. Figure 4 shows a comparison of adaptive calibration parameters vs. fixed parameters during heavy precipitation. The results are significantly better when $nsigma_z$ and phase are allowed to vary. Again, the paper does not fully describe why. The refractive index of the medium should be non dispersive (frequency independent), so it is difficult to justify that this effect is due to different propagation delays in the medium itself, as hinted in the paper. The only explanation left is the same as the previous section: the calibration parameters are part of the radar range image model – not fully independent radar calibration parameters independent of the radar target.

Response: In Fig. 4, we show the approach to mitigate the discontinuity of the imaging when precipitation echoes are significant. We found the phase bias, derived from the calibration approach, was different slightly between precipitation and atmospheric echoes. In view of this, respective values of phase biases obtained from the calibration process were employed to produce a more continuous imaging structure for the precipitation. This processing is effective for precipitation echoes.

The cause of difference in phase bias between precipitation and refractivity fluctuations is still unknown. We agree that the propagation delay in the medium should be the same for atmospheric and precipitation echoes. Therefore, we give another plausible conjecture in the last paragraph of Sect. 4.1, that is, the spatially inhomogeneous distribution and temporally quick change of the discrete-natured precipitation particles in the radar volume, which may lead to a breakdown of the assumptions for calibration of RIM data. The assumption for calibration of RIM data is that the atmospheric structures are continuous at the common edges of two adjacent range gates. This assumption may not be true for discrete targets such as precipitation particles.

One more cause we suspect is the different echoing mechanisms between precipitation and atmospheric scatterer. That is, the echoes of precipitation might have some phase shift from that of atmospheric scatterer. This needs a further theoretical study on the echo mechanism of precipitation.

In range imaging, there is no need to model the structure of targets (atmospheric scatterer and precipitation). The retrieved brightness can represent the power distribution of the targets in the range direction. All calibration results are valid for using the Capon method and the continuity assumption. With other retrieval methods or breakdown of the assumption, we may get different calibration scenes. This implies again the necessity of calibrating the RIM data for various radar parameters, retrieval methods, targets, and so on. We suppose that the range imaging model mentioned by the reviewer is associated with the optimization method.

Evaluation of multifrequency range-imaging technique implemented on the Chung-Li VHF atmosphere radar

J.-S. Chen[1,*], S.-C. Tsai[2], C.-L. Su[3], Y.-H. Chu[3]

[1]Center for General Education, China Medical University, Taichung, Taiwan

[2]Department of Environmental Information and Engineering, National Defense University, Taoyuan, Taiwan

[3]Institute of Space Science, National Central University, Jhongli, Taiwan

Corresponding to: J.-S. Chen (james.chen@mail.cmu.edu.tw)

Abstract

Multifrequency range imaging technique (RIM) has been implemented on the Chung–Li VHF array radar since 2008 after its renovation. This study made a more complete examination and evaluation of the RIM technique to facilitate the performance of the radar for atmospheric studies. RIM experiments with various radar parameters such as pulse length, pulse shape, receiver bandwidth, transmitter frequency set, and so on, were conducted. The radar data employed for the study were collected from 2008 to 2013. It has been shown that two factors, the range/time delay of the signal traveling in the media and the standard deviation of Gaussian-shaped range-weighting function, play crucial roles in ameliorating the RIM-produced brightness (or power distribution); the two factors are associated with some radar parameters. In addition to the radar parameters used, aging of cable lines or key components of the radar system resulted in an increase of the range/time delay of signal. It is also found that the range/time delay was slightly different for the echoes from the atmosphere with and without the presence of significant precipitation. A procedure of point-by-point correction of range/time delay was thus executed to minimize the bogus brightness discontinuity at range gate boundaries. With the RIM technique, the Chung–Li VHF radar demonstrates its first successful observation of double-layer structures as well as their temporal and spatial variations with time.

1 Introduction

The mesosphere–stratosphere–troposphere (MST) radar operated at very-high-frequency (VHF) band is a powerful instrument to study the atmosphere from near the ground up to the ionosphere. Among the capabilities of VHF-MST radar, continuous measurement of three-dimensional winds with a temporal resolution of several minutes and a vertical resolution of several hundred meters is praiseworthy (Lee et al., 2014). In addition to the air motion characterized by the wind field, small-scale structures of refractivity irregularities, such as thin layers with the thickness of tens of meters, exist commonly in the atmosphere and can reflect dynamic behavior of the atmosphere directly. However, a conventional atmosphere radar that operates at a specific frequency and a finite pulse length is unable to resolve the thin layer structures embedded within the range gate. In view of this, a frequency-hopped technique was introduced to the pulsed radar to overcome this limitation (Franke, 1990). The frequency-hopped technique was initially implemented with two frequencies on the VHF-MST radar, which can only resolve a Gaussian-shaped single layer in the range gate. Implementation of the frequency-hopped technique with more than two frequencies was not achieved until 2001 for ultra-high-frequency (UHF) wind profiler (Platteville 915MHz radar at 40.19^{o}N, 104.73^{o}W) (Chilson et al., 2003, 2004). Since then, the European incoherent scatter (EISCAT) VHF radar, the middle and upper atmosphere radar (MUR; 34.85^{o}N, 136.10^{o}E), the Ostsee wind (OSWIN) VHF radar (54.1^{o}N, 11.8^{o}E), the Chung–Li VHF radar (24.9^{o}N, 121.1^{o}E), and so on, also implemented this technique to observe gravity waves, double-layer structures, Kelvin–Helmholtz instability billows, convective structures, polar mesosphere summer echoes (PMSE), and so on, with high resolution in the range direction (e.g., Fernandez et al., 2005; Luce et al., 2006, 2008; Chen and Zecha, 2009; Chen et al., 2009). The terminologies of range imaging (RIM) (Palmer et al., 1999) and frequency-interferometric imaging (FII) (Luce et al., 2001) were given to the frequency-hopped technique for the radar remote sensing of the atmosphere. Some advanced applications of RIM have also been proposed, e.g., a high-resolution measurement of wind field in the sampling gate (Yu and Brown, 2004; Chilson et al., 2004; Yamamoto et al., 2014). Moreover, three-dimensional imaging of the scattering structure in the radar volume has been put into practice by combing RIM and coherent radar imaging (CRI) techniques (Hassenpflug et al., 2008; Chen et al., 2014a). Recently, some efforts on the calibration process of radar echoes were made to improve the performance of RIM (Chen et al., 2014b).

In this study, a large amount of RIM data that were collected by the Chung–Li VHF radar with various pulse lengths and shapes, phase codes, receiver bandwidths, frequency sets,

and so on, for the period from 2008 to 2013 were analyzed to evaluate the capability of the RIM technique implemented on the radar. It has been shown that the performance of RIM for the thin layer measurement relies on a proper calibration of the radar data, including time delay of radar signal, signal-to-noise ratio (SNR), and the range weighting function effect (Chen and Zecha, 2009). The time delay of the radar signal traveling in the media, such as the cable lines, free space, and processing time in the radar system, leads to a range delay and thereby gives a range error in the RIM processing. Besides, the range weighting function effect on the spatial distribution of the RIM-produced brightness is also required to adequately correct to restore the fine structures in the radar volume (Chen et al., 2014b). To this end, the calibration approach proposed by Chen and Zecha (2009), which is more convenient for our analysis, was employed in this study.

This article is organized as follow. In Sect. 2, the RIM capability of the Chung–Li VHF radar is introduced briefly. Section 3 gives an example of RIM as well as its calibration results for different radar parameters such as receiver system and frequency set. Section 4 presents the observations of precipitation and some layer structures. It is found that the time delay measured for precipitation echoes was different slightly from that of clear-air turbulences. A deeper examination was made to improve the RIM-produced brightness for precipitation echoes. In addition, double-layer structures and finer parts within the structures were resolved successfully to demonstrate the capability of RIM implemented on the radar system. Conclusion is drawn in Sect. 5.

2 Range-imaging technique of the Chung-Li VHF radar

The Chung–Li VHF radar system, operated at a central frequency of 52 MHz, has been upgraded for several years and carried out some valuable studies for the atmosphere (Chu et al., 2013; Su et al., 2014). In addition to a great improvement in radar signal processing, various pulse shapes such as rectangular, Gaussian, and trapezoid are available, and typical pulse widths are 1, 2 and 4 μs, yielding range gate resolutions of 150, 300, and 600 m, respectively. In addition, the range step can be as small as 50 m for oversampling (Chen et al., 2014b). Corresponding filter bandwidths can be chosen to match the transmitted pulse widths and pulse shapes. Barker and complementary codes are available to raise the signal-to-noise ratio of the received echoes, and more than five frequencies with a frequency step as small as 1 Hz can be set. These renovations and improvements in the radar characteristics enable the newly upgraded Chung–Li VHF radar to use the RIM technique to observe finer structures in

the atmosphere. The first experiment of RIM made with the Chung–Li radar was conducted successfully in 2008 (Chen et al., 2009), and since then many experiments with the RIM mode have been carried out by the radar. Table 1 lists many of the observations and their calibration results that will be discussed later. As listed, 1 and 2 μs pulse lengths, three types of pulse shapes, and different bandwidths and frequency sets were tested. Moreover, three receiving channels (subarrays) were functioned for reception of radar echoes. The analysis of various kinds of radar data can help us to realize the capability of the RIM technique implemented on the radar system for atmospheric measurements. A possible drawback of RIM may arise from the relatively broad radar beamwidth (~7.4^{o}), which smears the measured structure imaging due to a noticeable curvature of the radar beam.

In the RIM processing, the Capon method (Palmer et al., 1999), one of the optimization methods, was employed to estimate the range-dependent brightness. Although other optimization methods such as maximum entropy (Yu and Palmer, 2001) and multiple signal classification (Luce et al., 2001) are usable for RIM, the Capon method is simple, less consumption of time, and robust for the processing of radar data (Yu and Palmer, 2001). To acquire proper imaging of refractivity structures, corrections of range error and range weighting function effect are essential. In this study, we employed the calibration approach given by Chen and Zecha (2009) to make necessary corrections, which has been successfully tested for the Chung–Li radar and the MUR (Chen et al., 2009). The estimator of mean square error that is used to determine the optimal parameters for correcting the RIM-produced brightness is given by:

$$\Delta B = \sum_{i=1}^{N} \frac{(B_{1i} - B_{2i})^2}{B_{1i} B_{2i}} \tag{1}$$

where B_{1i} and B_{2i} are two sets of RIM-produced brightness values in the overlapped sampling range intervals of two adjacent range gates. N is the number of brightness values. Although the echoing structures in the overlapped sampling range intervals are the same and are supposed to have similar B_1 and B_2 values, the estimated B_1 and B_2 values may not be close to each other owing to two factors: sampling range error and range-weighting effect. Therefore, B_1 and B_2 values are expected to approximate to each other after the two factors are mitigated. In the calibration process, the optimal mitigation of the two factors gives a smallest value of ΔB, which is achieved by changing iteratively the sampling range error and the standard

deviation of the Gaussian-shaped range-weighting function in computing.

3 Observations and Calibrations

Table 1 lists sixteen cases of RIM experiments that were carried out between 2008 and 2013 by using the Chung–Li VHF radar. With the plentiful radar data, the long term variation in some of the characteristics of radar system will be addressed and discussed. In addition, the RIM experiments conducted on 9 November 2009 (cases 9 and 10) are presented as typical cases for specific demonstration in the following.

3.1 Different receiver systems

Figure 1 shows the statistical results of the calibration-estimated phase bias (left panels) and standard deviation σ_z (right panels) of the Gaussian range weighting function $\exp(-r^2/\sigma_z^2)$, where r is the range relative to the gate center, for the radar data of case 10. Only the atmospheric echoes with the SNR larger than -9 dB were analyzed and presented in Fig. 1. Note that the phase bias is a value transformed from the relationship: range delay×360°/range gate interval. Therefore, in this case the phase bias of 360^o corresponds to a range delay of 150 m or a time delay of 0.5 μs for the signal propagation.

As shown in Fig. 1, the phase bias histograms of the three receiving channels were in consistent with each other. The mean phase biases were centered at around 1230^o (peak location), corresponding to a range delay of 512.5 m or a time delay of ~1.708 μs. Note that some data with low SNR caused randomly distributed phase biases with numbers much less than that at peak location. In general, the distributions of phase biases for all of the RIM experiments listed in Table 1 were centered at their respective mean values, and the mean values of the three receiving channels were nearly the same. In view of this, the three receiver systems are thought to be approximately identical in conducting the RIM experiment. This, however, does not mean that the system phase difference between receiving channels, which is a crucial parameter for spatial radar interferometry, is close to zero. Similarity of phase bias distributions between different receiving channels suggests that the range/time delay be not the main cause of the system phase difference, if exists, between receiving channels of the Chung–Li radar. This issue is needed to clarify by other means and will not be discussed further in this study.

Figure 1b presents scatter diagrams of phase bias (left) and σ_z (right) vs. SNR,

respectively. As shown, for the data with SNR> 0 dB, the phase biases distributed majorly in a range of 1080–1440°, centered at around 1230°. By contrast, the σ_z values were SNR dependent, as seen in the right panel of Fig. 1b. A curve has been determined to represent the relationship between σ_z and SNR (Chen and Zecha, 2009), which is beneficial to produce the structure at gate boundaries with smoother imaging and is given below:

$$\sigma_z = \frac{1}{\frac{a}{(SNR+10)^c}+b} - d\,, \tag{2}$$

where the four constants a, b, c, and d are given in the plot (reading from top to bottom). The fitting curve reveals that the σ_z value tends to approach to a constant value of about 100 m, as the SNR increases. This curve-approached σ_z value at high SNR was close to the peak location of σ_z histogram (~115 m) shown in the right panels of Fig. 1a. The σ_z value at large SNR or the peak location of σ_z histogram can describe the theoretical shape of the Gaussian range weighting function. As derived in the previous studies (Franke, 1990), the standard deviation of the Gaussian range weighting function is given by $0.35c\tau/2$, where c is the speed of the light and τ is the pulse width. This value is obtained for a rectangular pulse shape used with its matched filter; for example, 52.5 m for 1-μs pulse width. According to our definition of Gaussian range weighting function, however, σ_z equals to $\sqrt{2}\times 0.35c\tau/2$, namely, about 74 m for 1-μs pulse width. This number is smaller than the calibrated value (100 m or 115 m). This is because that the case presented in Fig. 1 employed a Gaussian instead of rectangular pulse shape, resulting in a range-weighting function broader than that defined by the standard deviation of 74 m. By contrast, a trapezoid pulse shape that is close to a rectangular shape was employed in the case 8, thereby resulting in the value of 80 m for the peak location of σ_z that is not far from the value of 74 m. As for the dependence of σ_z value on SNR, it is not unaccountable because the performance of the Capon method is also SNR-dependent (Palmer et al., 1999, Yu et al., 2001). As the SNR decreases, the RIM brightness becomes less accuracy. In addition, there should be less and less thing to image as the SNR gets lower. As a result, the range-weighting effect becomes unimportant and a larger value of σ_z is obtained from the calibration process for a lower SNR case. It shoud be reminded that the relationship curve for σ_z and SNR could vary with the optimization method of range imaging; the calibration results

exhibited in this paper are valid only for the Capn method.

3.2 Time- and radar parameter-dependent characteristics

As revealed in Table 1, the peak location of phase bias varied with time. For 1 μs pulse length, the peak location was larger in 2013 than in 2009. For 2 μs pulse length the peak locations obtained in 2011 and 2012 were evidently larger than those obtained in 2008. The increase in phase bias with time is presumably due to the aging of cable lines or some components in the radar system that causes additional time delay of signal. As shown in Figure 2, the time delay estimated from the phase bias of receiver 1 (Rx_1) indeed has a tendency to increase with time. Nevertheless, those values of time delays for 1 μs pulse length in 2009 were obviously larger than the level indicated by the increasing tendency of time delay. It is thus worthy of additional investigation in the future to learn whether the radar system responds to different pulse lengths to result in various time delays; this can provide us a fully understanding of the characteristics of the radar system or other fundamental factors. .

On the other hand, the peak location of σ_z histogram, $\sigma_{z,peak}$, was not time dependent. Instead, it is a function of pulse shape and filter bandwidth; for example, the three radar experiments (cases 2–4) conducted on 11 April 2008 with different pulse shapes and filter bandwidths that were set alternately in the experiments (Chen et al., 2009). The experiment with Gaussian-shaped pulse and 250 kHz bandwidth (case 2) had a larger $\sigma_{z,peak}$ than that with squared pulse shape but the same filter bandwidth (case 3), and also larger than that with the same pulse shape but 500 kHz bandwidth (case 4), indicating a dependence of σ_z value on radar pulse shape as well as receiver bandwidth.

More examples are the radar experiments carried out on 27 July and 9 November in 2009 (cases 8–10). The radar parameters of 1 μs pulse length and 1 MHz filter bandwidth employed in the three experiments were the same, but the frequency sets and the pulse shapes were different. The trapezoid shape employed in the case 8 is a modified square pulse with a suppression of the sharp slopes at rising and falling edges of the pulse. We shall show later that the number of frequencies was not the main cause of variation in $\sigma_{z,peak}$ when the number of frequencies was more than five. However, the pulse shape plays a role in determining the $\sigma_{z,peak}$ value, in which the trapezoid pulse shape resulted in a smaller value of $\sigma_{z,peak}$. In addition, the peak location of phase bias on 27 July was smaller than that on 9 November by about 50^o; again, we attribute it to the aging of cable lines or some components in the radar system.

It is noteworthy that the experiment (case 7) carried out on 12 September 2008 used 7 bit Barker codes for pulse coding, with other radar parameters the same as the first RIM experiment conducted on 30 March 2008. There were no noticeable differences in the calibration results between the two cases. Moreover, the radar system was stable in 2008 because the peak locations of phase biases were in general agreement with each other.

3.3 Different frequency sets

RIM exploits an advantage of frequency diversity. The number of carrier frequencies and the frequency step play crucial roles in determining the performance of RIM. Figure 3 compares the histograms of the calibration-estimated phase biases and σ_z values at different frequency sets and frequency steps with the radar data of case 10. As shown, except for the two-frequency mode with the frequency pair (51.5, 52.5) MHz, all of other histograms had distinct peaks with locations at around 1240^o. This result clearly demonstrates that our calibration process is a robust approach to estimate the range/time delay of signal in the media and/or radar system. It can also be seen from Fig. 3 that the more the carrier frequency number is used, and the smaller the frequency separation is given, the more concentrated the distributions of phase biases and σ_z values will be. A closer examination shows that the peak locations of σ_z histograms approximate to a value of 120 m as the number of carrier frequencies increases.

In light of the fact that the performance of estimating the phase bias and the σ_z value is superior with more carrier frequencies and smaller frequency step, we exhibit the RIM results of cases 9 and 10 to demonstrate finer atmospheric layer structures within the range gates, as shown in Fig. 4. The left panels of Fig. 4 shows the original height time-intensity (HTI) plots with a range resolution of 150 m, and the right panels displays the RIM-produced brightness distributions with an imaging step of 1 m. In Fig. 4, there were some unknown interferences appeared periodically throughout range height but in short time interval. There were also many echoes from airplanes, which were strong but limited within short range and time interval. Ignoring these questionable echoes, a large number of thin layer structures with thickness as small as 30m or less can be observed from the RIM-produced brightness distributions. The temporal and spatial variations of the thin layer structures were characterized by dynamic behavior, with the features of prominent wavy structure (e.g., below the range height of 2.5 km in the panel a), descending or ascending gradually with time, and sudden occurrence or disruption of the layers at specific heights (e.g., between the range

heights of 5.0 and 6.0 km in the time interval of 4.0 and 5.0 h). In addition, double-thin layer structures with a separation as small as 100m or less can also be resolved (e.g., between the range height of 3.5 and 4.0 km in the panel b); we will discuss this type of layer structure in more detail in next section.

4 More observations and discussion

4.1 RIM for precipitation echoes

The calibration approach employed in the preceding section for RIM is based on the assumption that the atmospheric structures are continuous at the common edges of two adjacent range gates. With this assumption, the RIM-produced brightness at the common edges should be nearly identical after the two factors of range/time delay and range weighting function effect are compensated. This assumption is basically valid for random fluctuations of the atmospheric refractivity at the Bragg scale that serve as the scatterers to generate the radar returns. However, the continuity assumption may not be true for discrete targets such as precipitation particles. In such situation of discrete targets, the RIM-produced brightness did not vary smoothly through gate boundaries even the calibrated parameters were applied. One example observed on 21 August 2013 is shown in Fig. 5. In the plot, we should ignore the pulse-like echoes occurring quasi-periodically at range heights around 7 km, which were due to the airplanes landing on nearby airport. On the other hand, the strong echoes in the time interval between 5.5 h (05:30 UT) and 5.75 h (05:45 UT), and at around 5.0 h, were not only from the continuous refractivity fluctuations, but also from discrete precipitation particles. This feature can be verified from the power spectra of radar echoes as well as the rain rate measured by the disdrometer located near the radar site, as shown in Fig. 6. The rain rate in Fig. 6a shows two peak intensities occurred during the periods between 04:54 UT (4.9 h) and 05:06UT (5.1 h) and between 05:30 UT (5.5 h) and 05:42UT (5.7 h). The rainfall rate was alleviated between the two periods, and then almost vanished after ~05:42 UT. In Fig. 6b, three typical power spectra of radar echoes with and without precipitation are shown; the corresponding times of these power spectra are indicated sequentially by the red arrows in Fig. 6a. In the rightmost panel of Fig. 6b, the Doppler velocities were around zero throughout the altitude; it is clear that the echoes were generated by refractivity fluctuations without the contribution from precipitation particles. By contrast, Doppler velocities with large negative values were observed in the middle panel, which were associated with heavy rain. Note that

the rainfall velocity was so large that Doppler aliasing happened. The leftmost panel shows the condition of moderate precipitation, in which the spectral power of precipitation was much lower than that of refractivity fluctuations.

After range imaging with the constant phase bias indicated in Table 1, the RIM produced brightness in the middle panel of Fig. 5 exhibits evident discontinuities at the boundaries of range gates in the periods when intense precipitations occurred. The occurrence of discontinuity of the RIM-produced brightness at gate boundaries is presumably due to improper phase bias (range error) compensating in the RIM processing. When adaptable phase bias was adopted for each estimate of brightness, we obtained a better result as shown in the lowest panel of Fig. 5. As seen, discontinuity of the RIM-produced brightness through gate boundaries has been mitigated for precipitation echoes. In the following, we illustrate the necessity of using adaptable phase bias for precipitation echoes.

Figure 7a shows the histograms of phase biases and σ_z values for the data shown in Fig. 5. The overall features of the histograms of phase biases and σ_z values are similar to those shown in Fig. 1, except for the peak location of phase biases. Normalized distributions of phase biases and σ_z values varying with range gates are shown in the panel b. In general, the phase biases centered at around 1400^o. However, some phase biases with values smaller than 1400^o by as far as 90^o can be observed in the range interval between 11th and 25th range gates. An examination shows that these phase biases were associated with intense precipitation echoes. . On the other hand, the distributions of σ_z values were quite consistent throughout the entire range gates. Accordingly, adaptable phase bias for correction of range/time error is required to produce a more continuous imaging structure; the result is shown in the lowest panel of Fig. 5.

The cause of difference in phase bias between precipitation and refractivity fluctuations is still unknown. A plausible conjecture is spatially inhomogeneous distribution and temporally quick change of the discrete-natured precipitation particles in the radar volume, which may lead to a breakdown of the assumptions for calibration of RIM data. This issue may be investigated and clarified by using the technique of multi-receiver coherent radar imaging (CRI) (Palmer et al., 2005). Unfortunately, the Chung–Li radar does not have enough receiving channels for CRI technique and we need other suitable radars with CRI capability to conduct the radar experiment to tackle the problem of difference in phase bias between precipitation and refractivity fluctuations.

4.2 Double-layer structures

As shown in Fig. 4, various thin layer structures can be resolved by using the RIM technique. In this sub-section, two kinds of double-thin layer structures are inspected. In the lower panel of Fig. 8a, a stable double-thin layer structure separated by about 0.2 km was observed in the range interval between 3.2 km and 3.6 km, which cannot be resolved by the original HTI shown in the upper panel of Fig. 8a. The physical processes involved in the generation of the double-thin layer structure are Kelvin–Helmholtz instability (KHI) or vertically propagating wave breaking, both of which are associated with strong wind shear occurred in a very narrow range extent. Strong turbulence mixing is expected to occur in the double-layer structure due to dynamically instability, which leads to an enhancement of perturbation of the atmospheric refractivity and causes intermittent occurrences of the relatively intense echoes between the two layers. The lower panel of Fig. 8b presents another type of double-thin layer structure that is characterized by temporal merging and separation of the upper and lower thin layers, and shows much finer height-time structure than the original HTI displayed in the upper panel of Fig. 8b. Notice that, possibly being subject to a broad beam width (~7.4^{o}) of the Chung–Li VHF radar that may smear the RIM-produced brightness due to a limitation of poor horizontal resolution, the billow structures associated with the KHI were difficult to identify.

5 Conclusions

The Chung–Li VHF radar initiated multifrequency experiment in 2008, giving the capability of range imaging (RIM) for detecting finer atmospheric structures in the radar volume. Plenty of radar data have been collected since then, using different radar parameters such as pulse length, pulse shape, receiver bandwidth, transmitter frequency set, and so on. With these radar data, the RIM technique has been evaluated widely. Various kinds of thin layer structures with thickness of tens of meters were resolved by RIM even though the broad beamwidth of the radar beam may smear the echoing structures. For example, double-thin layer structures having occurrences of intense echoes within the two layers have been resolved for the first time of the Chung–Li VHF radar.

With the calibration process of RIM conducted in this study, it is found that the typical range/time delay of the signals can be obtained with only two-frequency data as long as the frequency separation of the two frequencies was small. For deriving the optimal range-weighting function, however, the use of seven carrier frequencies with 0.125MHz frequency step resulted in much more accurate outcomes than the use of two carrier frequencies. A

remarkable finding is that the longer the operating hours of the radar system is, the larger the range/time delay will be; this feature is presumably attributed to the aging of cable lines or components in the radar system. One more important finding in this study is a visible shift of range delay when precipitation echoes are significant, which causes the problem of discontinuity in the RIM-produced brightness at range gate boundaries. We propose in this article a process of point-by-point correction of range error to mitigate the brightness discontinuity to improve the imaging quality of the RIM-produced structures for precipitation environment.

Based on the capability of the RIM technique in resolving finer atmospheric structures, it is expected that RIM can help us to reveal more detailed information on the topics of special atmospheric phenomena, such as tremendously thin layer structure, minute turbulence configuration and spatial precipitation distribution in the radar volume. It is also expected in the future that the RIM technique can be applied to the ionosphere for observing plasma density fluctuations in meteor trail as well as field aligned plasma irregularities. High resolution at about several meters may reveal the delicate structure of plasma irregularities in more detail, which can hopefully help us to understand the temporal evolution of plasma instability at the very beginning stage.

Acknowledgements

This work was supported by the Ministry of Science and Technology of ROC (Taiwan), Grants MOST103-2111-M-039-001 and MOST104-2111-M-039-001. The Chung–Li VHF radar is maintained by the Institute of Space Science, National Central University, Taiwan.

References

Chen, J.-S. and Zecha, M.: Multiple-frequency range imaging using the OSWIN VHF radar: phase calibration and first results, Radio Sci., 44, RS1010, doi:10.1029/2008RS003916, 2009.

Chen, J.-S., Su, C.-L., Chu, Y.-H., Hassenpflug, G., and Zecha, M.: Extended application of a novel phase calibration method of multiple-frequency range imaging to the Chung–Li and MU VHF radars, J. Atmos. Ocean. Tech., 26, 2488–2500, 2009.

Chen, J.-S., Furumoto, J., and Yamamoto, M.: Three-dimensional radar imaging of atmospheric layer and turbulence structures using multiple receivers and multiple

frequencies, Ann. Geophys., 32, 899–909, doi:10.5194/angeo-32-899-2014, 2014a.

Chen, J.-S., Su, C.-L., Chu, Y.-H., and Furumoto, J.: Measurement of range-weighting function for range imaging of VHF atmospheric radars using range oversampling, J. Atmos. Ocean. Tech., 31, 47–61, 2014b.

Chilson, P. B., Yu, T.-Y., Strauch, R. G., Muschinski, A., and Palmer, R. D.: Implementation and validation of range imaging on a UHF radar wind profiler, J. Atmos. Ocean. Tech., 20, 987–996, 2003.

Chilson, P. B.: The retrieval and validation of Doppler velocity estimates from range imaging, J. Atmos. Ocean. Tech., 21, 987–996, 2004.

Chu, Y.-H., Yang, K-.F., Wang, C.-Y., and Su, C.-L: Meridional electric fields in layer-type and clump-type plasma structures in mid-latitude sporadic E region: observations and plausible mechanisms, J. Geophys. Res.-Space Physics, 118, 1243-1254, doi:10.1002/jgra.50191, 2013.

Fernandez, J. R., Palmer, R. D., Chilson, P. B., Häggström, I., and Rietveld, M. T.: Range imaging observations of PMSE using the EISCAT VHF radar: Phase calibration and first results, Ann. Geophys., 23, 207–220, doi:10.5194/angeo-23-207-2005, 2005.

Franke, S. J.: Pulse compression and frequency domain interferometry with a frequency-hopped MST radar, Radio Sci., 25, 565–574, 1990.

Hassenpflug, G., Yamamoto, M., Luce, H., and Fukao, S.: Description and demonstration of the new Middle and Upper atmosphere Radar imaging system: 1-D, 2-D and 3-D imaging of troposphere and stratosphere, Radio Sci., 43, RS2013, doi:10.1029/2006RS003603, 2008.

Lee, C. F., Vaughan, G., and Hooper, D. A.: Evaluation of wind profiles from the NERC MST radar, Aberystwyth, UK, Atmos. Meas. Tech., 7, 3113–3126, doi:10.5194/amt-7-3113-2014, 2014.

Luce, H., Yamamoto, M., Fukao, S., Hélal, D., and Crochet, M.: A frequency radar interferometric imaging (FII) technique based on high-resolution methods, J. Atmos. Sol. Terr. Phys., 63, 221–234, 2001.

Luce, H., Hassenpflug, G., Yamamoto, M., and Fukao, S.: High-resolution vertical imaging of the troposphere and lower stratosphere using the new MU radar system, Ann. Geophys., 24, 791–805, doi:10.5194/angeo-24-791-2006, 2006.

Luce, H., Hassenpflug, G., Yamamoto, M., Fukao, S., and Sato, K.: High-resolution observations with MU radar of a KH instability triggered 5 by an inertia-gravity wave in the upper part of a jet stream, J. Atmos. Sci., 65, 1711–1718, 2008.

Palmer, R. D., Yu, T.-Y., and Chilson, P. B.: Range imaging using frequency diversity, Radio Sci., 34, 1485–1496, doi:10.1029/1999RS900089, 1999.

Palmer, R. D., Cheong, B. L., Hoffman, M. W., Fraser, S. J., and López-Dekker, F. J.: Observations of the small-scale variability of precipitation using an imaging radar, J. Atmos. Ocean. Tech., 22, 1122–1137, doi:10.1175/JTECH1775.1, 2005.

Su, C.-L., Chen, H.-C., Chu, Y.-H., Chung, M.-Z., Kuong, R.-M., Lin, T.-H., Tzeng, K.-J., Wang, C.-Y., Wu, K.-H., and Yang, K.-F.: Meteor radar wind over Chung-Li (24.9°N, 121°E), Taiwan, for the period 10–25 November 2012 which includes Leonid meteor shower: Comparison with empirical model and satellite measurements, Radio Sci., 49, doi:10.1002/2013RS005273, 2014.

Yamamoto, M. K., Fujita, T., Aziz, N. H. B. A., Gan, T., Hashiguchi, H., Yu, T.-Y., and Yamamoto, M.: Development of a digital receiver for range imaging atmospheric radar, J. Atmos. Sol.-Terr. Phy., 118, 35–44, 2014.

Yu, T.-Y., and Palmer, R. D.: Atmospheric radar imaging using spatial and frequency diversity. *Radio Sci.,* **36,** 1493–1504, 2001.

Yu, T. Y. and Brown, W. O. J.: High-resolution atmospheric profiling using combined spaced antenna and range imaging techniques, Radio Sci., 39, RS1011, doi:10.1029/2003RS002907, 2004.

Yu, T.-Y., Furumoto, J., and Yamamoto, M.: Clutter suppression for high-resolution atmospheric observations using multiple receivers and multiple frequencies, Radio Sci., 45, RS4011, doi:10.1029/2009RS004330, 2010.

Table Captions

Table 1: RIM experiments of the Chung–Li VHF radar and calibration results.

Figure Captions

Figure 1: (a) Histograms of the calibrated parameters for three independent receiving channels. Phase bin is 20^{o} and σ_z bin is 10 m. The shapes and sizes of the three receiving arrays are the same. (b) Scatter plot of the calibrated parameters vs. SNR for the second receiving channel (Rx_2). The curve describing the relationship between σ_z and SNR is a fitting curve for correcting the RIM-produced brightness. Data time: 06:49:27 UT – 08:49:47 UT, 9 November 2009.

Figure 2: Time delays in different time periods. Refer to Table 1 for the observational time period of each case.

Figure 3: Histograms of the calibrated parameters for different sets of transmitter frequencies, with the radar data collected from the second receiving channel (Rx_2) in Fig. 1. The values quoted at the title locations are the transmitter frequencies; the unit is MHz.

Figure 4: (a) (Left) High-time intensity with a range resolution of 150 m, and (right) range imaging with a range step of 1 m. (b) is similar to (a), but the radar data were collected later on the same day (9 November 2009).

Figure 5: (upper) High-time intensity with a range resolution of 150 m, and (middle and bottom) RIM-produced brightness with, respectively, constant and adaptive values of range error in the correction process. Imaging range step is 1 m. Data time: 21 August 2013.

Figure 6: (a) Rain rate measured by the disdrometer located near the radar site. (b) Three typical power spectra of radar echoes at the times indicated sequentially by the red arrows in (a).

Figure 7: (a) Histograms of the calibrated parameters for the radar data shown in Fig. 4. (b) Normalized distributions of the calibrated parameters at different range gates. The value attached at right side of each gate is mean SNR in dB of that gate.

Figure 8: Two types of double-layer structures observed on 9 November 2009. In (a, b) both, the upper and lower panels show, respectively, height-time intensity and RIM-produced brightness.

Table 1: RIM experiments of the Chung-Li VHF radar and calibration results.

Case	Exp. date (hh:mm, UT)	Pulse length (μs) /shape/code or oversampling	Filter band-width (kHz)	Freq set (MHz)/ Freq. No.	Sampling time (s)	Calibration results: Peak location of phase bias/$\sigma_{z,peak}$ *Range delay/time delay*		
						Rx_1	Rx_2	Rx_3
1	2008/03/30 (17:05-24:00)	2/s	500	f_a/5	0.256	320°/160 m *(267m/0.889μs)*	320°/180 m	330°/170 m
2	2008/04/11a (02:50-04:20)	2/g	250	f_a/5	0.256	350°/260 m *(292m/0.972μs)*	340°/250 m	350°/260 m
3	2008/04/11b (02:50-04:20)	2/s	250	f_a/5	0.256	325°/210 m *(271m/0.903μs)*	340°/200 m	330°/210 m
4	2008/04/11c (02:50-04:20)	2/g	500	f_a/5	0.256	340°/210 m *(283m/0.944μs)*	350°/210 m	350°/220 m
5	2008/09/12a (02:54-05:17)	2/s	250	f_a/5	0.256	345°/220 m *(288m/0.958μs)*	350°/220 m	350°/220 m
6	2008/09/12b (02:54-05:17)	2/s	250	f_b/5	0.256	340°/220 m *(283m/0.944μs)*	350°/225 m	350°/220 m
7	2008/09/12c (06:12-07:15)	2/s/7-bit Barker	500	f_a/5	0.32	320°/180 m *(267m/0.889μs)*	315°/160 m	320°/170 m
8	2009/07/27 (05:30-08:23)	1/T	1000	f_d/5	0.512	1180°/80 m *(492m/1.639μs)*	1180°/85 m	1200°/80 m
9	2009/11/09a (03:08-05:38)	1/g	1000	f_e/7	0.1792	1230°/115 m *(513m/1.708μs)*	1230°/115 m	1250°/115 m
10	2009/11/09b (06:49-08:49)	1/g	1000	f_f/7	0.1792	1230°/115 m *(513m/1.708μs)*	1230°/115 m	1240°/120 m
11	2011/12/02 (03:39-05:52)	2/g/over	500	f_a/5	0.128	500°/210 m *(417m/1.389μs)*	505°/200 m	505°/200 m
12	2012/01/05 (02:22-04:56)	2/s/over	500	f_a/5	0.128	500°/150 m *(417m/1.389μs)*	500°/150 m	500°/150 m
13	2012/01/05 (04:59-07:38)	2/s/over	1000	f_a/5	0.128	520°/135 m *(433m/1.444μs)*	520°/140 m	530°/140 m
14	2012/08/08a (05:32-07:02)	2/s/over	500	f_c/7	0.1792	610°/160 m *(508m/1.694μs)*	620°/160 m	615°/160 m
15	2012/08/08b (07:07-08:37)	2/s/over	500	f_g/7	0.1792	610°/150 m *(508m/1.694μs)*	615°/160 m	615°/150 m
16	2013/08/21 (00:00-07:00)	1/g	1000	f_d/5	0.128	1410°/110 m *(586m/1.958μs)*	1420°/110 m	1410°/110 m

f_a: 51.75, 51.875, 52.0, 52.125, 52.25
f_b: 51.75, 51.8, 52.0, 52.1, 52.25
f_c: 51.75, 51.8, 51.875, 52.0, 52.1, 52.125, 52.25
f_d: 51.5, 51.75, 52, 52.25, 52.5
f_e: 51.5, 51.6, 51.75, 52.0, 52.2, 52.25, 52.5
f_f: 51.5, 51.75, 51.875, 52, 52.125, 52.25, 52.5
f_g: 51.75, 51.833334, 51.916667, 52.0, 52.083333, 52.166666, 52.25
pulse shape: g≡Gaussian, s≡square, T≡Trapezoid
over: oversampling with a range step of 50 m

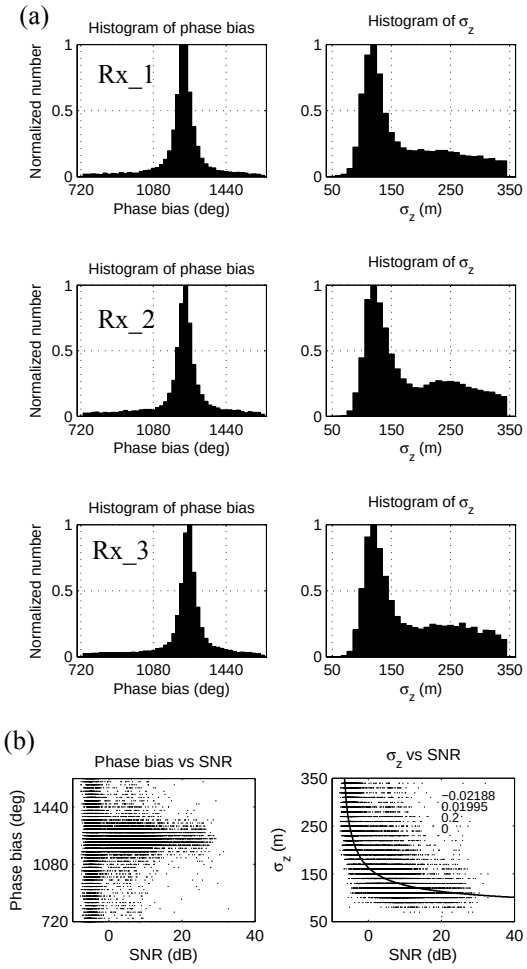

Figure 1: (a) Histograms of the calibrated parameters for three independent receiving channels. Phase bin is 20^{o} and σ_z bin is 10 m. The shapes and sizes of the three receiving arrays are the same. (b) Scatter plot of the calibrated parameters vs. SNR for the second receiving channel (Rx_2). The curve describing the relationship between σ_z and SNR is a fitting curve for correcting the RIM-produced brightness. Data time: 06:49:27 UT – 08:49:47 UT, 9 November 2009.

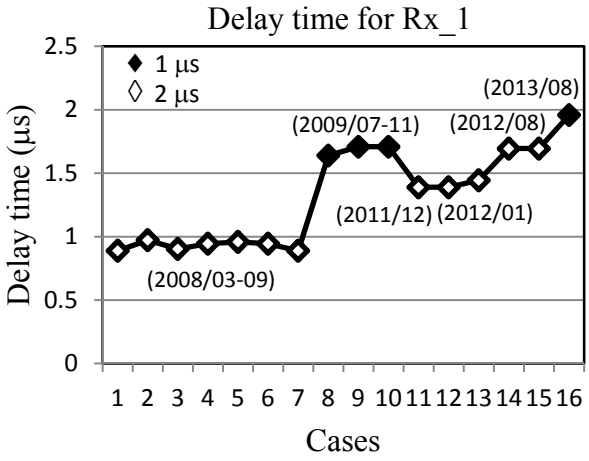

Figure 2: Delay times in different time periods. Refer to Table 1 for the observational time period of each case.

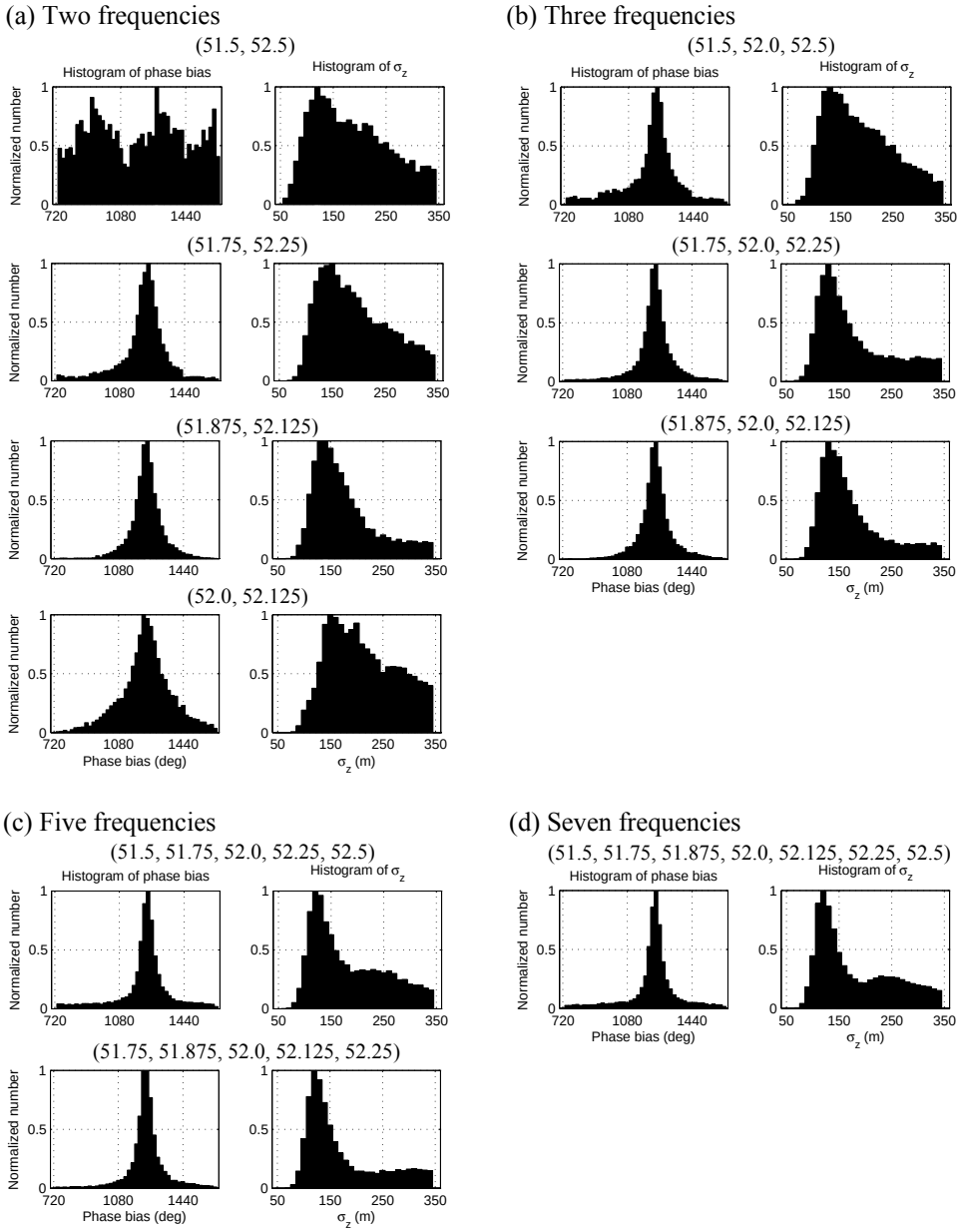

Figure 3: Histograms of the calibrated parameters for different sets of transmitter frequencies, with the radar data collected from the second receiving channel (Rx_2) in Fig. 1. The values quoted at the title locations are the transmitter frequencies; the unit is MHz.

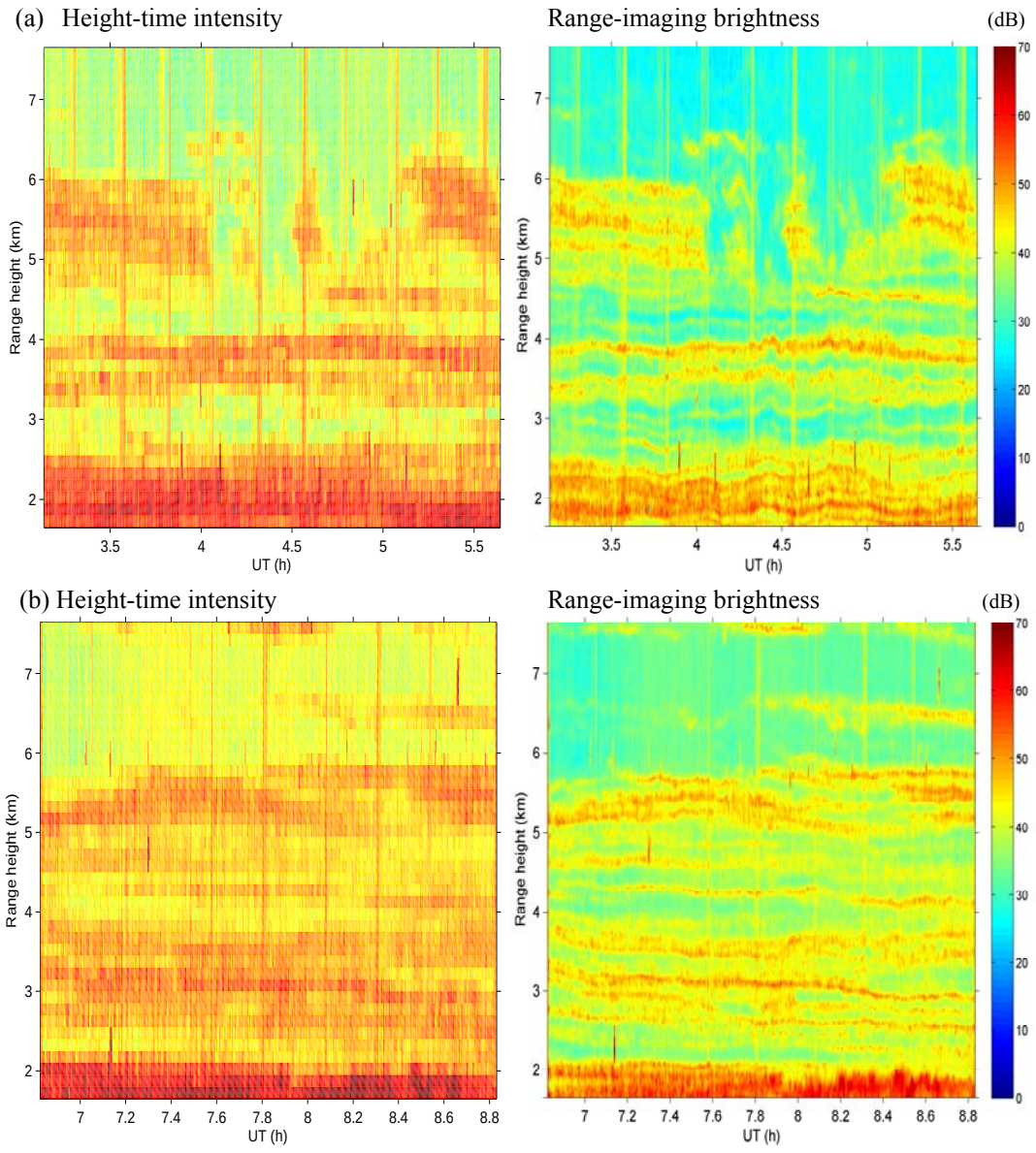

Figure 4: (a) (Left) High-time intensity with a range resolution of 150 m, and (right) range imaging with a range step of 1 m. (b) is similar to (a), but the radar data were collected later on the same day (9 November 2009).

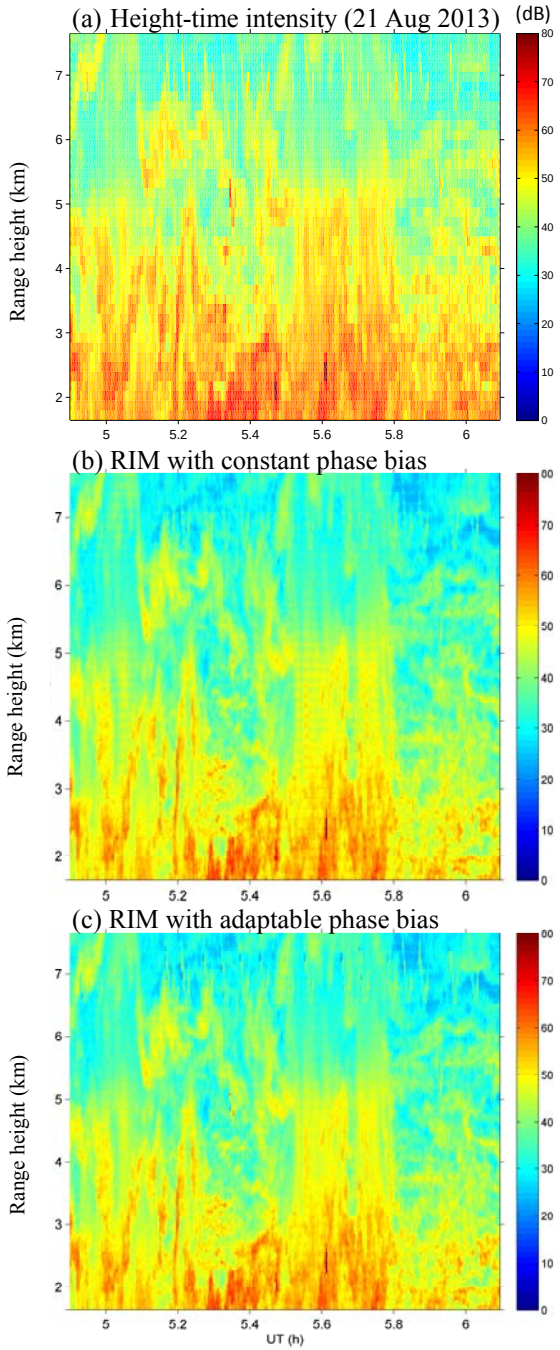

Figure 5: (a) High-time intensity with a range resolution of 150 m, and (b, c) RIM-produced brightness with, respectively, constant and adaptive values of range error in the correction process. Imaging range step is 1 m. Data time: 21 August 2013.

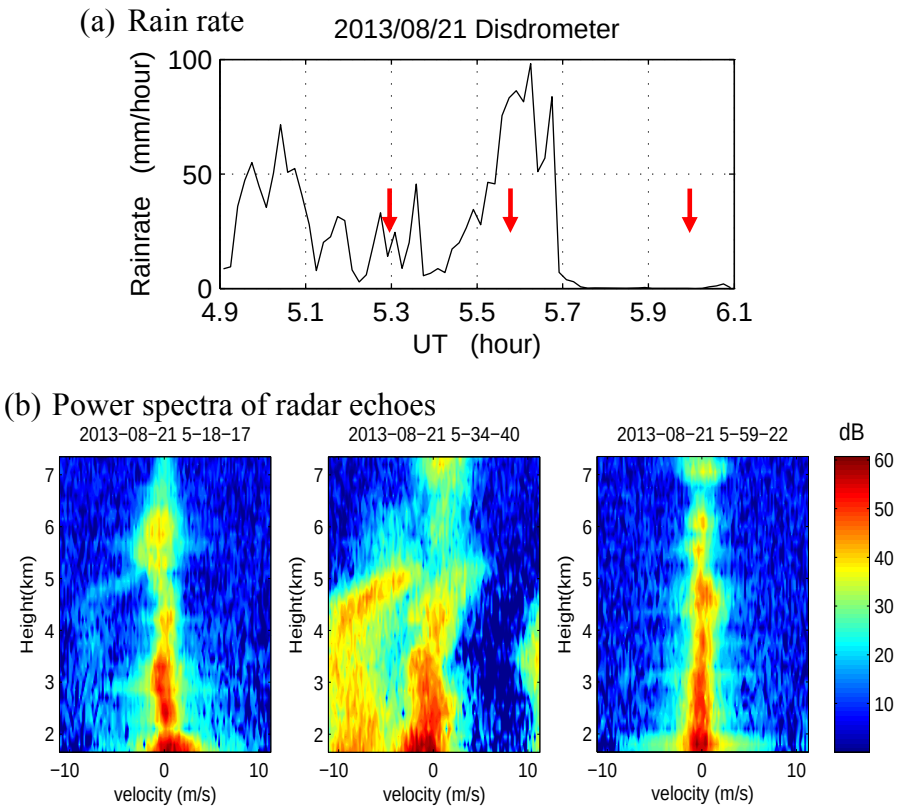

Figure 6: (a) Rain rate measured by the disdrometer located near the radar site. (b) Three typical power spectra of radar echoes at the times indicated sequentially by the red arrows in (a).

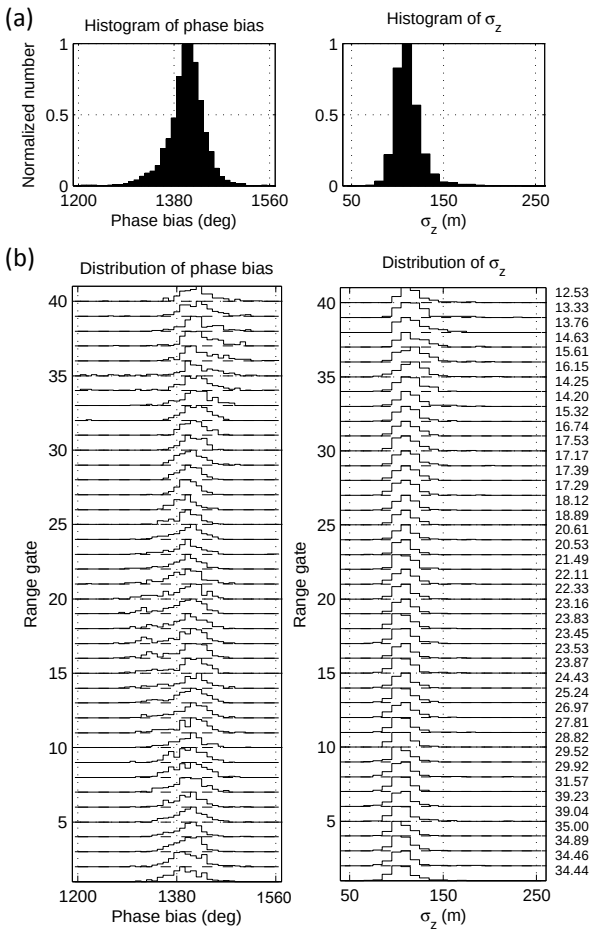

Figure 7: (a) Histograms of the calibrated parameters for the radar data shown in Fig. 4. (b) Normalized distributions of the calibrated parameters at different range gates. The value attached at right side of each gate is mean SNR in dB of that gate.

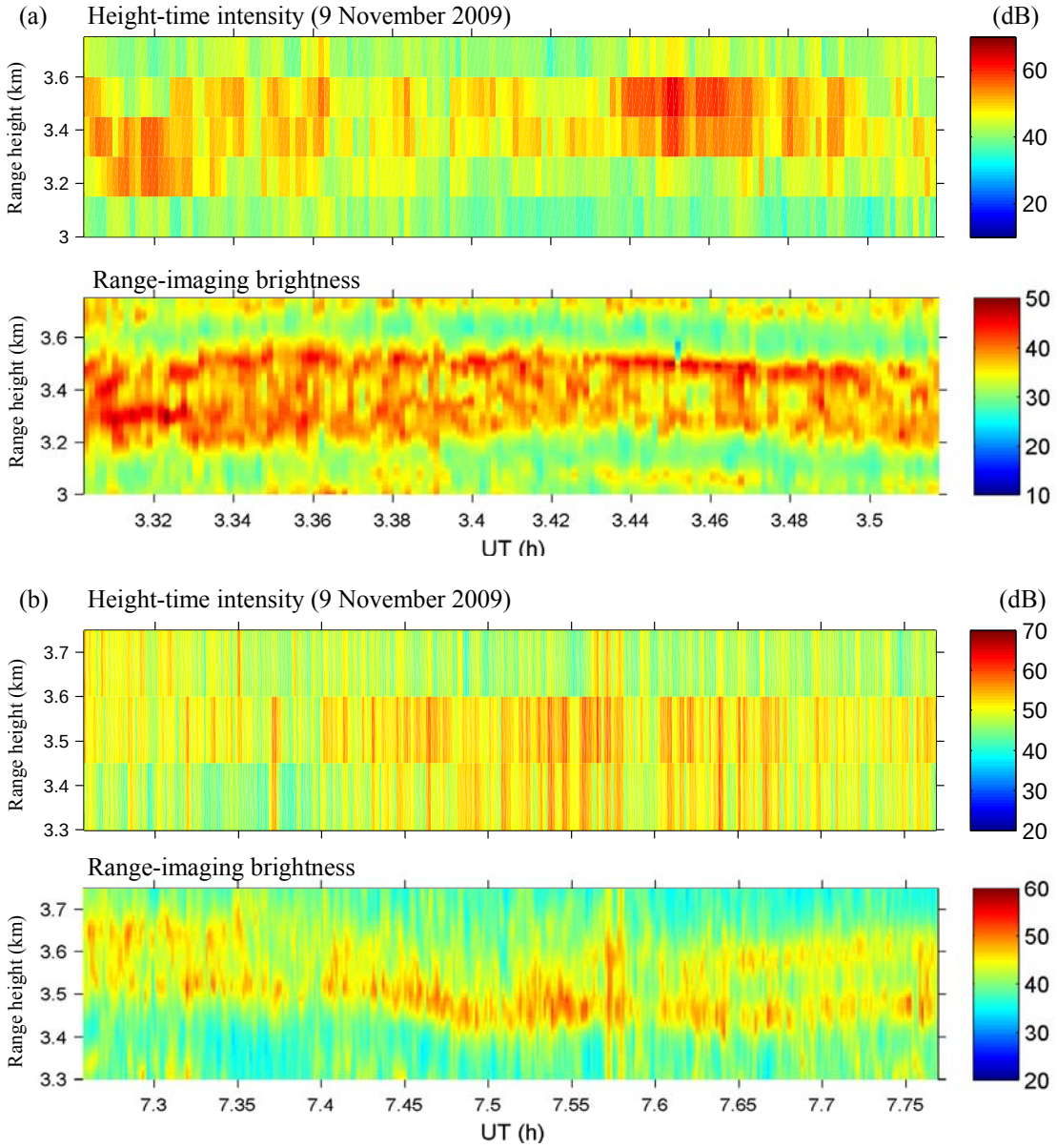

Figure 8: Two types of double-layer structures observed on 9 November 2009. In (a, b) both, the upper and lower panels show, respectively, height-time intensity and RIM-produced brightness.